



THE UNIVERSITY *of* EDINBURGH

Edinburgh Research Explorer

Pore-scale imaging of hydrogen displacement and trapping in porous media

Citation for published version:

Thaysen, EM, Butler, IB, Hassanpouryouzband, A, Freitas, D, Alvarez-borges, F, Krevor, S, Heinemann, N, Atwood, R & Edlmann, K 2022, 'Pore-scale imaging of hydrogen displacement and trapping in porous media', *International journal of hydrogen energy*. <https://doi.org/10.1016/j.ijhydene.2022.10.153>

Digital Object Identifier (DOI):

[10.1016/j.ijhydene.2022.10.153](https://doi.org/10.1016/j.ijhydene.2022.10.153)

Link:

[Link to publication record in Edinburgh Research Explorer](#)

Document Version:

Publisher's PDF, also known as Version of record

Published In:

International journal of hydrogen energy

Publisher Rights Statement:

© 2022 The Author(s). Published by Elsevier Ltd

General rights

Copyright for the publications made accessible via the Edinburgh Research Explorer is retained by the author(s) and / or other copyright owners and it is a condition of accessing these publications that users recognise and abide by the legal requirements associated with these rights.

Take down policy

The University of Edinburgh has made every reasonable effort to ensure that Edinburgh Research Explorer content complies with UK legislation. If you believe that the public display of this file breaches copyright please contact openaccess@ed.ac.uk providing details, and we will remove access to the work immediately and investigate your claim.

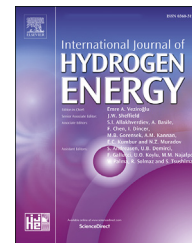




ELSEVIER

Available online at www.sciencedirect.com

ScienceDirect

journal homepage: www.elsevier.com/locate/he

Pore-scale imaging of hydrogen displacement and trapping in porous media

Eike M. Thaysen ^{a,*}, Ian B. Butler ^a, Aliakbar Hassanpouryouzband ^a,
Damien Freitas ^a, Fernando Alvarez-Borges ^b, Samuel Krevor ^c,
Niklas Heinemann ^a, Robert Atwood ^b, Katriona Edlmann ^a

^a School of Geoscience, Grant Institute, The King's Buildings, The University of Edinburgh, James Hutton Road, Edinburgh, EH9 3FE, United Kingdom

^b Diamond Light Source Ltd, Harwell Campus, Didcot OX11 0DE, United Kingdom

^c Department of Earth Science and Engineering, Imperial College London, London SW7 2AZ, United Kingdom

HIGHLIGHTS

- Hydrogen injectivity and recovery in rock is imaged with x-ray computed micro-CT.
- Hydrogen recovery decreases with increasing reservoir depth.
- Hydrogen recovery increases with increasing brine flow rate.
- Hydrogen trapping occurs via snap-off processes.
- Nitrogen is a poor proxy for hydrogen.

ARTICLE INFO

Article history:

Received 11 July 2022

Received in revised form

25 September 2022

Accepted 16 October 2022

Available online xxx

Keywords:

Geological hydrogen storage

μ CT

Porous media

Recovery

Drainage

Imbibition

ABSTRACT

Hydrogen can act as an energy store to balance supply and demand in the renewable energy sector. Hydrogen storage in subsurface porous media could deliver high storage capacities but the volume of recoverable hydrogen is unknown. We imaged the displacement and capillary trapping of hydrogen by brine in a Clashach sandstone core at 2–7 MPa pore fluid pressure using X-ray computed microtomography. Hydrogen saturation obtained during drainage at capillary numbers of $<10^{-7}$ was $\sim 50\%$ of the pore volume and independent of the pore fluid pressure. Hydrogen recovery during secondary imbibition at a capillary number of 2.4×10^{-6} systematically decreased with pressure, with 80%, 78% and 57% of the initial hydrogen recovered at 2, 5 and 7 MPa, respectively. Injection of brine at increasing capillary numbers up to 9.4×10^{-6} increased hydrogen recovery. Based on these results, we recommend more shallow, lower pressure sites for future hydrogen storage operations in porous media.

© 2022 The Author(s). Published by Elsevier Ltd on behalf of Hydrogen Energy Publications LLC. This is an open access article under the CC BY license (<http://creativecommons.org/licenses/by/4.0/>).

* Corresponding author.

E-mail address: eike.thaysen@ed.ac.uk (E.M. Thaysen).

<https://doi.org/10.1016/j.ijhydene.2022.10.153>

0360-3199/© 2022 The Author(s). Published by Elsevier Ltd on behalf of Hydrogen Energy Publications LLC. This is an open access article under the CC BY license (<http://creativecommons.org/licenses/by/4.0/>).

Introduction

The storage of surplus electrical energy could increase the utility of renewable energy sources thereby reducing the environmental impact of energy generation [1,2]. Storage mediums like batteries, compressed air, capacitors, or fly-wheels are only applicable for the short-term and small-scale electricity storage [3]. The use of hydrogen (H_2) as an energy vector however could provide long-term storage to balance the intermittent demand and supply challenges affecting renewable methods [3]. Considering the low energy density of H_2 [4], storage of H_2 in large storage sites is the only solution for economical, gigawatt to terawatt-scale H_2 storage. Underground storage of H_2 in salt caverns is an established technology [5], yet, only subsurface porous media (saline aquifers and depleted oil and gas fields), can provide TWh storage capacities that could balance seasonal demands [4]. Relative to cavern storage, inter-seasonal storage in porous media is poorly understood and introduces a range of other complexities [2], including potential pore-clogging by microbial growth [6], gas loss out of diffuse lateral boundaries, viscous fingering of H_2 into reservoir brines, residual trapping and possible reactions with the primary formation fluid and reservoir minerals [7–9]. Each of these requires consideration of multiphase flow, transport and reaction [2,7].

Recent years have seen several studies on H_2 geochemistry [10–14] and the elucidation of many important flow characteristics of H_2 including; Hydrogen relative permeability and capillary pressure [15–18], interfacial tension (IFT) [19–21], and H_2 /brine/rock contact angles [16,19,20,22–28]. Despite these advances important unknowns remain, e.g. the amount and type of cushion gas required in different geological settings, the risk for H_2 leakage via lateral boundaries and wells, the extent of microbial clogging and hydrogen consumption, and the degree of capillary trapping of H_2 as a function of pore size distribution.

Amongst the remaining unknowns, capillary trapping, which leads to a reduced volume of recoverable H_2 , in this way impacting the economic feasibility of the H_2 storage operation, is of principal relevance [7]. Pore scale observations are particularly valuable for the assessment of capillary trapping [24]. Additional data describing the H_2 fluid flow and capillary trapping in different porous formations and under varying conditions are vital to make accurate predictions of the H_2 plume development and to define optimum production strategies [7]. The capillary forces that control capillary trapping also control the relative permeability [7]. As such studies on residual trapping give insight to a range of crucial input parameters for pore-scale and reservoir H_2 storage models.

The effects of the brine pore fluid pressures and of brine flow rate on capillary trapping of H_2 are hitherto unknown. The brine pore fluid pressure is linked to the reservoir depth via the hydrostatic gradient, hence an investigation of the latter could facilitate the definition of an optimal storage depth for gas recovery. The flowrate affects the capillary number, N_c , via equation (1):

$$N_c = \frac{q \cdot \mu}{\sigma} \quad (1)$$

where q is the flow, μ is the viscosity of the invading fluid and σ is the interfacial tension (IFT). As N_c increases, viscous forces dominate capillary forces and capillary trapping of the non-wetting phase decreases [29]. This capillary desaturation with increasing N_c , depends on the rock type [30] and on the kind of nonwetting phase [29] and is observed around critical capillary numbers of 10^{-5} to 10^{-8} [29].

A non-destructive standard technique for visualization and analysis of wetting and non-wetting phase displacement processes in porous media is x-ray micro-computed tomography (μ CT) [31]. Pore-scale models are directly reliant on μ CT images to build up the basic models for appropriate understanding of gas storage operations [32]. Previously published μ CT studies on two-phase flow in porous media involving gas have largely focused on supercritical carbon dioxide (sCO_2) in sandstones and limestones. Reported saturations of sCO_2 in non-aged (i.e. not wettability altered by exposure to oil or organic acids) water-wet rocks range from 30 to 60% during drainage and from 15 to 30% during imbibition, at N_c between 10^{-8} to 10^{-6} and 10^{-8} to 2×10^{-5} , respectively [31,33–36]. Studies using subcritical, gaseous carbon dioxide (CO_2), which could be more readily compared to H_2 , are scarce. Yet, the characteristic trapping curves for sCO_2 and CO_2 , which show the residual saturation (S_{nwr}) as a function of initial saturation (S_{nwi}), are not significantly different [37]. Saturations of nitrogen (N_2) during drainage and imbibition in sandstones with 6–22% porosity are 43–64% and 43%, respectively, at N_c between 1.7×10^{-8} [38,39]. Carbon dioxide trapping increases at lower pressures due to decreasing water contact angles [40]. Unlike in CO_2 storage, trapping is not desirable in geological H_2 storage as it leads to unrecoverable H_2 .

Some observational studies have suggested that H_2 is less wetting on rocks than CO_2 [23,25]. At the time of writing four μ CT studies, one micro-model study and one nuclear magnetic resonance (NMR) study on H_2 exist: Al-Yaseri et al. (2022) [41] used NMR to find H_2 S_{nwi} and S_{nwr} of 4% and <2%, respectively, in a Fontainebleau sandstone at 0.4 MPa and ambient temperature. Higgs et al. (2021) [19] μ CT-imaged H_2 injection into a 5 mm diameter and 7.6 mm length core of Bentheimer sandstone at pressures of 6.8–20.8 MPa and documented decreasing IFT between H_2 and water with increasing pressure (72.5 mN m^{-1} at 6.9 MPa to 69.4 mN m^{-1} at 20.7 MPa). Jha et al. (2021) [42] conducted a single cycle H_2 -brine displacement sequence in a 5 mm diameter and 15 mm length core of Gosford sandstone, and used μ CT to calculate an S_{nwi} of 65% during drainage and a S_{nwr} of 41% after brine imbibition. Rock samples in Jha et al. (2021) [42] and Higgs et al. (2021) [19] were sufficiently short for capillary end effects to dominate the flow behaviour, where the wetting phase accumulates close to the production face of the core [43]. The experiment by Jha et al. (2021) [42] was performed at ambient pressure and leaves open the question of variations in H_2 wetting and flow behaviour at reservoir conditions [23]. Increasing pore fluid pressures have been reported to increase the gas saturation and pore network connectivity for N_2 in a brine wet, aged Bashijiqike tight sandstone (0.6% gas saturation at 2 MPa versus 43% at 8 MPa) [38]. The effect of increases in N_c from 7.7×10^{-7} to 3.8×10^{-4} on the H_2 flow through a sandstone micro-model at 0.5 MPa was investigated by Lysy

et al. (2022) [24] who found that S_{nwi} increased correspondingly from 18% to 79% [24]. Recently, Jangda et al. (2022) [44] reported S_{nwi} and S_{nwr} of 36% and 25%, respectively in unaged Bentheimer sandstone at 10 MPa and 50 °C [44]. In this work, we used μ CT to investigate the displacement and capillary trapping of H_2 by brine in 4.7 mm diameter and 54–57 mm length Clashach sandstone cores as a function of gas and brine pore fluid pressure (2–7 MPa) and flow rate (20–80 μ l min^{-1} , corresponding to H_2 and brine bulk N_c of $1.7-6.8 \times 10^{-8}$ and $1.2-9.4 \times 10^{-6}$, respectively). The objectives of this work were to 1) deduce the effect of pore fluid pressure on H_2 capillary trapping, where the pore fluid pressure can be related to injection pressure and reservoir pressure in a H_2 storage scenario, allowing the definition of optimum storage depths for H_2 recovery, and 2) deduce the effect of brine flow rates on H_2 capillary trapping, to determine if increased recovery is possible with increased flow rate.

We show that the H_2 S_{nwi} is independent of pore fluid pressure but that higher brine pore fluid pressures during secondary imbibition increase capillary trapping of H_2 , indicating decreased H_2 recovery at greater reservoir depths and hence less favourable conditions for H_2 storage. Higher flow rates during secondary imbibition on the other hand decrease capillary trapping, indicating that some trapped H_2 may be recovered under high flow conditions. Our work advances the current understanding of H_2 flow in porous media by delivering the first realistic estimates on how much H_2 can be recovered from the subsurface after injection, disregarding any H_2 loss by microbial or geochemical reactions, as a function of reservoir depth and flow rate.

Materials and methods

Core-flooding experiments

We performed unsteady and steady state, two-phase core flooding experiments with H_2 (purity 99.9995 vol%, BOC Ltd.) and brine (0.5 M CsCl or 2 M KI, Sigma-Aldrich) in a Clashach sandstone (Permian, aeolian sandstone from near Elgin in Scotland; the composition of Clashach is: ~96 wt% quartz, 2% K-feldspar, 1% calcite, 1% ankerite [45], porosity 11.1–14.4% [45–47]) at ambient temperature (~293 K). The Clashach sandstone, with its low mineralogical variability, yet still comparably big pore space, was chosen in order to facilitate the visualization of the injected H_2 and the interpretation of the results.

Two types of experiments were carried out: The first set of experiments (from now on referred to as UoE (University of Edinburgh) experiments) was carried out using the μ CT instrument at the University of Edinburgh and were aimed at imaging the displacement and capillary trapping of H_2 by brine as a function of saturation after drainage and imbibition under different experimental conditions. Three UoE experiments were carried out that investigated the effect of pore fluid pressure (2–7 MPa), whereof each was repeated once (UoE exp. 1–3, Table 1). The standard error on the H_2 saturation in the repeated experiments was calculated as the standard deviation divided by the square root of the number of repeated experiments. One UoE experiment looked at the

Table 1 – Overview over experiments.

Experiment	Type of x-ray source	Description	Sample	H_2 /brine injection ratio	Flowrate (μ l min^{-1})	Pore fluid pressure (MPa)	Confining pressure (MPa)	Pore volumes injected	Repetitions of experiment
UoE exp. 1	laboratory	Primary drainage and imbibition in unsteady state displacements of H_2 and brine	1	–	20	7	9	10	1 entire repetition, 1 repetition on drainage only
UoE exp. 2	laboratory	Primary drainage and imbibition in unsteady state displacements of H_2 and brine	1	–	20	5	9	10	1
UoE exp. 3	laboratory	Primary drainage and imbibition in unsteady state displacements of H_2 and brine	1	–	20	2	9	10	1
UoE exp. 4	laboratory	Simultaneous, steady state injections of H_2 and brine	1	1.4, 1.1, 4:1	20	5	9	10	–
UoE exp. 5	laboratory	Primary and secondary drainage and imbibition in unsteady state displacements of H_2 and brine	1	–	80	5	9	10	–
UoE exp. 6	laboratory	Unsteady state displacements of H_2 and brine	1	–	20	5	9	10	–
UoE exp. 7	laboratory	Unsteady state displacements of N_2 and brine	1	–	80	5	9	10	–
Dry rock	synchrotron	Unsteady state, brine injection into dry, H_2 saturated rock	2	–	5	5	10	10	–

effect of the H_2 /brine injection ratio on the H_2 saturation (UoE exp. 4, Table 1). This experiment was carried out to evaluate the effect of H_2 injection into aquifers with different magnitudes of brine flow (hydrodynamic aquifers), and to simulate the far field situation, where H_2 and brine move together. Another UoE experiment investigated the effect of secondary drainage and imbibition (UoE exp. 5, Table 1). UoE exp. 6 used N_2 instead of H_2 . This experiment was undertaken in order to compare the flow behaviour of the two gases, which is of relevance because N_2 is sometimes used as an analogue for H_2 , e.g. in permeability measurements [10,17]. Because rearrangement processes in the pore volume were noted previously for N_2 [38], UoE exp. 7 (Table 1) was undertaken to examine the stability of H_2 in the rock volume over an experimental duration (10 h): Ten PV of H_2 were injected into a brine-saturated rock while keeping the pressure constant inside the pressure vessel, with imaging undertaken at the start and after 10 h. The effect of bulk capillary number on drainage and imbibition was deduced by a comparison of the results from UoE exp. 2 and 5 which used flowrates of 20 and 80 $\mu\text{l min}^{-1}$, respectively, and 5 MPa injection pressure (Table 1).

The second type of experiment (from now on referred to as the 'dry rock experiment'; Table 1) used synchrotron radiation (Diamond Light Source, I12-JEEP tomography beamline) to capture the time-resolved displacement of H_2 by brine in a dry, H_2 -saturated rock. This experiment served as a base of comparison to the displacements of H_2 in wet, brine-saturated rock (UoE experiments). The chosen set of experiments allowed for the detailed assessment of the mechanisms behind H_2 and brine displacement processes in Clasach sandstone and allowed quantifying the hitherto unknown H_2 recovery from porous rock as a function of pressure/depth and flow.

All experiments used a bespoke x-ray transparent core holder for a 5 mm diameter rock core, which was a scaled-up version of the cell described by Fuisseis et al. (2014) [48]. In UoE experiments a carbon-fibre reinforced PEEK pressure vessel was used to permit good x-ray transparency. The dry rock experiment used an aluminium pressure vessel to comply with the health and safety requirements at Diamond Light Source. The specifications of the pressure vessels of PEEK and aluminium were engineered with safety factors of 2 times or more over and above the maximum applied confining pressure (10 MPa; Table 1).

Rock cores for the experiments were obtained by diamond drill coring with a water-flushed chuck, followed by preparation of the core ends by grinding on a lathe. Experiments used a set of four high-pressure pumps (Cetoni NemesysTM, flow-rate range 0.072 ml s^{-1} to 13.76 ml s^{-1}): One for the injection of H_2 , one for the injection of brine, one to hold the backpressure and one for the confining pressure (Fig. 1). A bespoke manifold system composed of high-pressure 1/8" and 1/16" 316 stainless steel and 1/16" PEEK tubing (Swagelok, Top Industrie and Cole Parmer, respectively) connected the pumps to the core-flood cell (Fig. 1). Additional pressure transducers (ESI Technology; accuracy 0.1% full-scale) were coupled to the flow system at the inlet and outlet to allow for higher precision pressure monitoring than was possible using the integral

pressure gauges in the syringe pumps. Cyclic H_2 and brine injections used a Clashach outcrop sample without further cleaning of 4.7 mm diameter and a relatively long length of 54–57 mm to avoid the influences of capillary end effects [49,50]. To prevent leakage of H_2 into the confining fluid, the rocks were jacketed in aluminium foil and polyolefin heat-shrink tubing and sealed with silicone adhesive between the conical-ended pistons within the pressure vessel. In UoE experiments, a water-wet rock was first saturated with brine (0.5 M CsCl) at a flow rate of 70 $\mu\text{l min}^{-1}$. Afterwards, H_2 was injected (drainage) into the brine-saturated rock at flow rates of 20–80 $\mu\text{l min}^{-1}$, based on desired capillary-regime N_c of 1.7–6.8 $\times 10^{-8}$ (The viscosity of H_2 is 9.01 $\mu\text{Pa s}$ at 298K and 4.7 MPa [51] and the IFT between H_2 and water is 72.6 mN m^{-1} at 298K and 5 MPa [52,53]). Subsequently, the brine was reinjected (imbibition) at flow rates of 20–80 $\mu\text{l min}^{-1}$, resulting in N_c of 2.4–9.5 $\times 10^{-6}$ (using the same IFT between H_2 and water of 72.6 mN m^{-1} at 5 MPa and 298 K [52,53] and a viscosity of 1.247 $\times 10^{-3}$ Pa s at 5 MPa that was estimated from the reported 1.2503 $\times 10^{-3}$ Pa s and 1.233 $\times 10^{-3}$ Pa s at 0.1 MPa and 25 MPa, respectively, and 298 K [54]). The N_c in the N_2 experiment was 3.5 $\times 10^{-8}$ during drainage (using an IFT of 73 mN m^{-1} between N_2 and water at 298K and 10 MPa [37] and a viscosity of 1.89 $\times 10^{-5}$ Pa s at 5 MPa and 295K [51]). Each injection used ten pore volumes to ensure complete flushing of the sample cores with the injected fluid.

In the dry rock experiment, H_2 was directly injected into a dry rock at a flow rate of 70 $\mu\text{l min}^{-1}$. Subsequently, the brine (2 M KI) was injected at a flow rate of 5 $\mu\text{l min}^{-1}$, resulting in N_c of 5 $\times 10^{-7}$ (using the same IFT between H_2 and water of 72.6 mN m^{-1} at 5 MPa and 298 K [52,53] and a viscosity of 1.07 $\times 10^{-3}$ Pa s for 0.6 M KI and 293 K [45]).

The combined application of an x-ray transparent core holder and μCT allowed the visualization of the fluid saturation distributions at pore scale at each injection step. The difference in the x-ray attenuation coefficient of the fluids (H_2 and 0.5 M CsCl/2 M KI) provided an excellent contrast between the two fluid phases and the rock on the acquired μCT images, combined with the respective radiation energy in the two different laboratories.

3D volumes were acquired from the lower central portion of the sample to avoid the impact of capillary end effects on fluid saturation [49,50]. For the UoE experiments, image acquisition used a μCT instrument built in-house at the University of Edinburgh, comprising a Feinfocus 10–160 kV reflection source, a Micos UPR-160-air rotary table and a PerkinElmer XRD 0822 1 MP amorphous silicon flat panel detector with a terbium doped gadolinium oxysulfide scintillator. Data acquisition software was developed in-house. The following settings were used for UoE experiments: 120 keV, 16 W, 2 s exposure time, 1200 projections and 2 frames per stop. The voxel size was 5.4 μm^3 . In the dry rock experiment, time-resolved imaging of the H_2 and brine displacement processes was achieved by means of a 65 keV monochromatic beam detected by a high-resolution imaging camera with optical module 2 (PCO.edge 5.5, 7.91 \times 7.9 $\mu\text{m}/\text{pixel}$ with FoV 20 mm \times 12 mm) using 17–25 ms exposure time and 900 projections. The voxel size was 7.9 μm^3 .

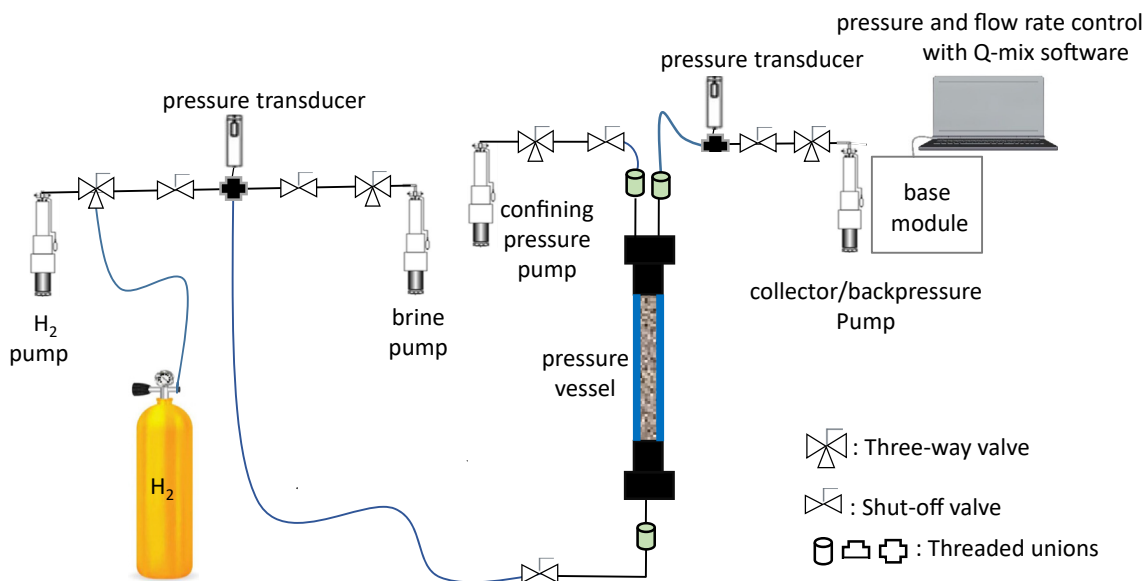


Fig. 1 – Experimental setup showing the manifold system that connected the X-ray transparent pressure vessel to a set of four high-pressure Cetoni Nemesys™ pumps: one to inject H₂, one inject brine, one to maintain backpressure and one to maintain confining pressure. The materials for the connections were 316 stainless steel (black), HPLC (green) and PEEK or carbon fibre reinforced PEEK (blue). The pressure vessel consisted of carbon fibre reinforced PEEK in UoE experiments and of aluminium in the dry rock experiment (see text). Pressure and flow rate control was achieved with the Q-mix software. (For interpretation of the references to color/colour in this figure legend, the reader is referred to the Web version of this article.)

Image analysis

Tomographic reconstructions were undertaken by filtered back projection using Octopus 8.9 [55] on a GPU accelerated workstation. All subsequent image processing and analysis of tomographic data was performed using Avizo Version 9.1.1 (FEI, Oregon, USA). Data from UoE experiments were processed using a non-local means filter [56]. Processing of the dry rock experiment used a combination of median filter and unsharp mask to reduce image noise. Segmentation of UoE experiment data used a global threshold on the 2D greyscale image histogram, and encompassed two phases. In the water-wet scans, water and rock were treated as two discrete phases. In scans after brine and H₂ injections, the H₂ was treated as one phase and the brine and rock as a single separate phase, following protocols of Andrew et al. (2014) [34]. Holes and spots which were at the resolution limit of the data were removed from all datasets (applied thresholds corresponded to 3³ and 5³ voxels, respectively). Based on the segmented image of the water-wet scan in UoE experiments, a pore size distribution was calculated. The 3D image was separated into discrete pores using Avizo's 'separate objects' module, which calculates a chamfer distance map of the pore-space and then applies a marker based watershed algorithm to the distance map to define discrete pore bodies as catchment basins, separated by the watershed which marks the location of pore throats (Figure A1d). Supporting information Fig. A1 shows the work flow for the water-wet scan.

In scans following brine and H₂ injections in UoE experiments, the segmented image was analysed in 3D using the 'labeling' and 'label analysis' modules to identify, label and measure the volume of each H₂ cluster. Hydrogen cluster size

distributions were compared to the pore size distribution to evaluate the H₂ connectivity and identify trapping mechanisms during brine imbibition.

Capillary pressure

Recovered Clashach cores were submerged in 25% w/v NaOH solution (Fisher Scientific) for 2 h to remove the aluminium foil from the core surface, and rinsed in successive Milli-Q water, acetone and ethanol ultrasonic baths. Subsequently, the cores were cut and squared to the dimensions of 25 mm, overlapping the μ CT visualized rock volumes, and cleaned ultrasonically with Milli-Q water to remove grinding products. Mercury injection capillary pressure (MICP) was performed on the cleaned cores, using a micromeritics automated mercury injection equipment (Autopore IV 9500) to estimate the capillary pressure-saturation relationship and pore size distribution. The pressure range tested was from vacuum to 379 MPa.

Results

Characterization of the pore space

The μ CT-evaluated porosity of the Clashach sandstone from the segmented volume of the water-wet rock was 12.5%–13.5%, depending on the imaged region of the rock core. The MICP-evaluated pore throat size distribution showed a large number of very small pore throats with <5 μ m radius and a small number of small to intermediate size pore throats (>5–90 μ m) (Fig. 2). The largest pore throat had a radius of

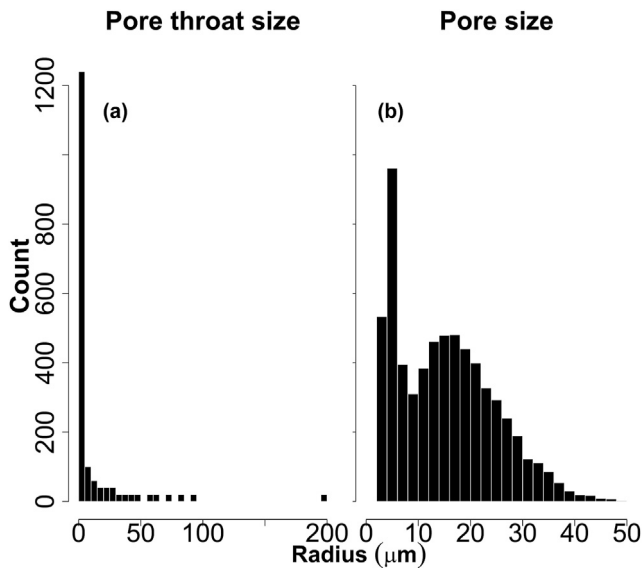


Fig. 2 – MICP-derived pore throat size distribution (a) and μ CT-derived pore size distribution (b) Note that MICP-derived counts were multiplied by a factor of 20 to facilitate visualization of the results. All plots used a bin size of 30.

195 μm (Fig. 2). The μ CT-evaluated size distribution of the pores evidenced a narrow pore size distribution with comparably small pores with radii $< 50 \mu\text{m}$ (Figs. 2 and 4a).

Hydrogen wetting behaviour and stability in UoE experiments

Hydrogen sat in the centre of the pore bodies. Residual brine sat in corners, pore throats (Fig. 3b and c) and, as a subtraction of the water saturated scan from the H_2 - and brine filled rock revealed, in thin films around the grains (Fig. 3d). The injected H_2 remained stable within the pore volume under no-flow conditions and at constant pore fluid pressure over a time period of 10 h which was the maximum experimental duration (Fig. A2).

Effect of pore fluid pressure on hydrogen connectivity, saturation and recovery

Hydrogen saturation during drainage was independent of the pore fluid pressure with 49.8%, 51.7% and 39.7%–52.6% saturation at pore fluid pressures of 2, 5 and 7 MPa, respectively (Fig. 4a–c, f, Fig. A3). Hydrogen connectivity during drainage generally showed one large, connected cluster at all pore fluid pressures except for one out of three images at 7 MPa which showed three large clusters (Fig. 5, Fig. A3). During drainage, the largest H_2 cluster had a volume of $1 \times 10^8 \mu\text{m}^3$ at all pore fluid pressures except for the one run at 7 MPa with the disconnected clusters were the largest volume was $7 \times 10^7 \mu\text{m}^3$ (Fig. 5e). Hydrogen clusters during drainage were at all pore fluid pressures much larger than discrete pores with a maximum volume of $1.3 \times 10^6 \mu\text{m}^3$ (Fig. 5e, a). Comparing all H_2 cluster size distributions during drainage (Fig. 5f) reveals that all drainage curves, including two of the distributions at 7 MPa (squares and rhombi), have largely the same

distribution, however one of the three distributions at 7 MPa (triangles) is distinct. This outlier experiment corresponds to the experiment showing a lower S_{nwi} (Fig. 4c).

Capillary trapping of H_2 during imbibition seemed independent of the pore fluid pressure with 10%, 12% and 4–21% of trapped H_2 at 2, 5 and 7 MPa, respectively (Fig. 4a–c, f, Fig. A3), corresponding to 20%, 22% and 11–43% of the initially injected H_2 . During imbibition, large H_2 clusters were broken down into smaller clusters (Fig. 5a–d), in line with the visual changes of the H_2 clusters (Fig. 4a–c and f). The largest H_2 clusters after imbibition remained above the maximum pore size during all experiments except for one experiment at 7 MPa (Fig. 5g and a), showing that not only was H_2 trapped in discrete pore bodies but also as larger H_2 ganglia. The break-down of the largest H_2 clusters during imbibition caused the number of clusters in the size range $\log 4$ to $\log 6 \mu\text{m}^3$ to increase while the number of very small clusters of $\log 2$ – $4 \mu\text{m}^3$ typically decreased (Fig. 5b–d). Comparing all H_2 cluster size distributions during imbibition (Fig. 5g) shows that the distributions at 2 and 5 MPa are largely the same while the imbibition distributions at 7 MPa are distinct.

Injections of H_2 and brine into the same rock volume and at the same flow rates and pore fluid pressures of 2–5 MPa were repeatable with small standard errors between 0.01 and 0.66% (Fig. 4a and b, Fig. 5b and c). At 7 MPa very distinct S_{nwi} and S_{nwr} were measured (Fig. 4c and f); During drainage the standard error was 4.8% at an average H_2 saturation of 47.4%. The standard error during imbibition was 8.5% at an average saturation of 12.9%. The pressure differences between inlet and outlet during the experiments were within the error of the pressure sensors of 0.1% full-scale.

Effect of hydrogen/brine injection ratio on hydrogen connectivity and saturation

We studied the effect of the H_2 /brine injection ratio on the H_2 saturation in order to evaluate the effect of H_2 injection into hydrodynamic aquifers, and to evaluate what happens in the far field, where fluids will be moving together. The results showed that the H_2 saturation and H_2 interconnected pore volume increased with increasing H_2 /brine injection ratio from 32.6% at $4 \mu\text{l min}^{-1}$ H_2 plus $16 \mu\text{l min}^{-1}$ brine to 43.2% at $16 \mu\text{l min}^{-1}$ H_2 plus $4 \mu\text{l min}^{-1}$ brine (Fig. 6). The H_2 clusters in simultaneous injection experiments occupied many of the same pore spaces as the clusters after H_2 in the unsteady state experiments at the same pressure and total flowrate (Figs. 4b and 6, Fig. A6), and even at the lowest H_2 brine injection ratio of $4 \mu\text{l min}^{-1}$ H_2 plus $16 \mu\text{l min}^{-1}$ brine, the H_2 clusters were large, and spanning multiple pores (Fig. 6a). The percolation threshold, i.e. one connected path from inlet to outlet, was apparently only reached at 100% H_2 injection (Fig. 4b vs. Fig. 6, Fig. A6). The pressure differences between inlet and outlet during the simultaneous injection experiments were up to 0.05 MPa.

The H_2 cluster volume distributions were similar at different H_2 :brine injection ratios (Fig. 7a). However, with increasing ratio the smallest H_2 clusters of volume $\sim \log 2 \mu\text{m}^3$ decreased in number while the number of intermediate size ($\log 2.5$ to $\log 6.25 \mu\text{m}^3$) H_2 clusters and the volume of the biggest cluster increased (Fig. 7a), confirming observations of

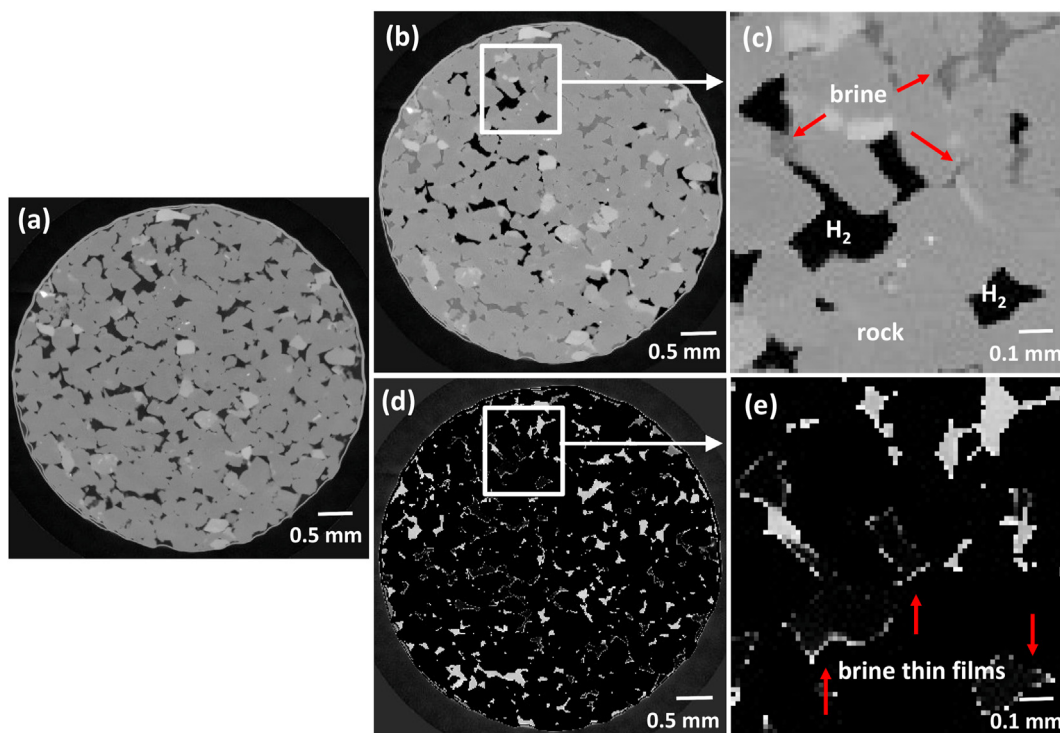


Fig. 3 – (a) Water-wet Clashach sandstone with the water shown in black and the rock in different shades of grey. (b) and (c) Brine-saturated Clashach sandstone after injection of H₂. H₂ (black) fills the centre of the pores while the brine (dark grey) remains in corners and small pore throats around grains (different shades of grey). (d) and (e) Subtraction of the water-wet scan from the brine-saturated scan after H₂ injection, following registration of the brine-saturated scan after H₂ injection to the water-wet scan, revealing discontinuous brine thin films around grains. The rim around the Al foil in (d) is caused by continued shrinkage of the Al foil onto the rock during the experiments. (For interpretation of the references to color/colour in this figure legend, the reader is referred to the Web version of this article.)

increasing H₂ saturation and connectivity with increasing injection ratio (Fig. 6).

Effect of flowrate on hydrogen saturation and recovery

At constant pore fluid pressure of 5 MPa, increases in the flowrate during drainage from 20 $\mu\text{l min}^{-1}$ to 80 $\mu\text{l min}^{-1}$, corresponding to bulk N_c of 1.7×10^{-8} to 6.8×10^{-8} , respectively, decreased the S_{nwi} from 51.7% to 47.7% (Fig. 4b and d). Correspondingly, increases in the brine flowrate during imbibition from 20 $\mu\text{l min}^{-1}$ to 80 $\mu\text{l min}^{-1}$, corresponding to bulk N_c of 2.4×10^{-6} and 9.4×10^{-6} , respectively, reduced the S_{nwr} from 11.5% to 7.2% (Fig. 4b and d).

In line with this, the H₂ cluster size distributions at the two flowrates showed that larger clusters were mobilized at 80 $\mu\text{l min}^{-1}$ (maximum cluster sizes of $\log 6.25 \mu\text{m}^3$ at 80 $\mu\text{l min}^{-1}$ vs. $\log 6.75 \mu\text{m}^3$ at 20 $\mu\text{l min}^{-1}$; Fig. 7b). At both flowrates the largest H₂ clusters were still bigger than the largest pore of $<\log 6 \mu\text{m}^3$ (Fig. 7b vs. Fig. 6a), indicating that H₂ was trapped also as larger ganglia.

Secondary drainage and tertiary imbibition

Secondary drainage and tertiary imbibition did not significantly change the H₂ saturation (47.9% and 7.0%) compared to primary drainage and secondary imbibition (47.6% and

7.3%), based on results at 5 MPa and 80 $\mu\text{l min}^{-1}$ flowrate (Fig. A4, Fig. 4d and e).

Dry rock experiment

In the dry-rock experiment, the brine entered the H₂-filled dry rock via piston-like displacement, (Fig. 8b), eventually recovering the H₂ entirely (Fig. 8d). Before all H₂ was recovered, there was an intermediate stage where previously brine-filled pores (Fig. 8b) showed several very small H₂ bubbles (Fig. 8d).

Comparison to nitrogen

The N₂ saturation was similar to the H₂ saturation during drainage (48.7% vs. $51.7 \pm 0.66\%$, respectively) but N₂ saturation after brine imbibition was much higher (33.9% vs. $11.5 \pm 0.64\%$, respectively; Fig. 4e, Fig.A5). The N_c of H₂ and N₂ during drainage was 1.7×10^{-8} and 3.5×10^{-8} , respectively.

Discussion

Pore space

The μCT -evaluated porosity of the Clashach sandstone from the segmented volume of the water-wet rock of 12.5–13.6%

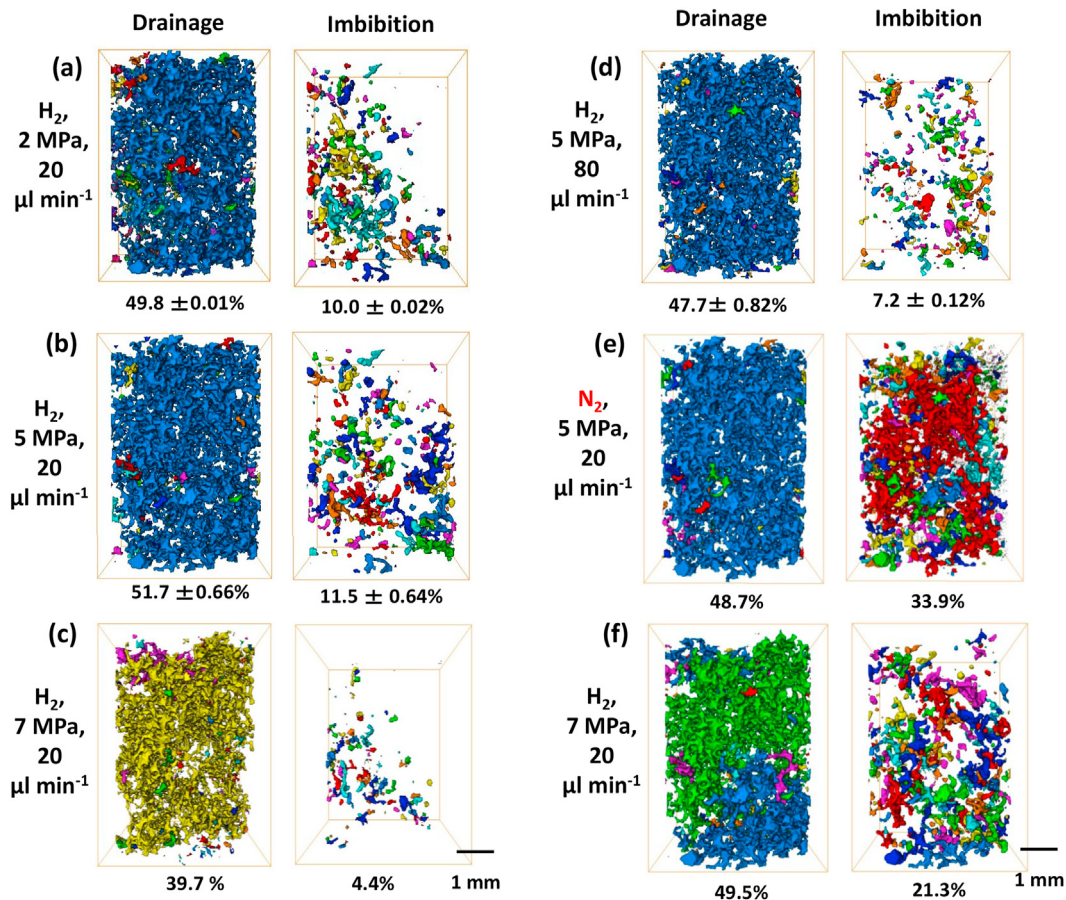


Fig. 4 – 3D rendering of H_2 and N_2 clusters with saturation percentages in UoE experiments. Discrete clusters were rendered in colors, where mainly one color marks one large, connected cluster and different colors indicate several, not connected clusters. (a–c) Effect of pore fluid pressure on H_2 clusters and H_2 saturation after drainage and secondary imbibition. (a) 2 MPa, (b) 5 MPa and (c, f) 7 MPa, all at a constant flow rate of $20 \mu\text{l min}^{-1}$, corresponding to capillary numbers of 1.7×10^{-8} and 2.4×10^{-6} during drainage and imbibition, respectively. Large, connected clusters that existed after drainage were broken down to numerous smaller clusters after imbibition, with apparently no clear relationship between H_2 saturation and pore fluid pressure. Experiments were repeated once at 2 and 5 MPa, and at 7 MPa twice for drainage runs and once for imbibition. For experiments at 2 MPa and 5 MPa averages and standard errors for the H_2 saturation are reported. For experiments at 7 MPa, due to the discrepancy in the results, both of the full primary drainage and imbibition experiments are visualized in (c) and (f). (d) Effect of cyclic injections on H_2 clusters and saturation: Averages and standard errors of the H_2 saturation after primary and secondary drainage, and after secondary and tertiary imbibition, all at 5 MPa pore fluid pressure and a flowrate of $80 \mu\text{l min}^{-1}$, corresponding to a capillary number of 9.4×10^{-6} . (e) Nitrogen clusters and saturations during drainage and imbibition at 5 MPa pore fluid pressure and a flowrate of $20 \mu\text{l min}^{-1}$. For the full display of the results see Fig. A3 and Fig A4. (For interpretation of the references to color/colour in this figure legend, the reader is referred to the Web version of this article.)

was within the range of the published porosities of 11.1–14.4% for Clashach sandstone [45–47]. The distributions of pore size and pore throat size as evaluated by μCT and MICP, respectively, suggested that mostly small pores of $<50 \mu\text{m}$ radii were joined by very small throats of $<5 \mu\text{m}$ radii with a few small to intermediate size throats of $>5\text{--}90 \mu\text{m}$ radii in between (Fig. 2). The largest pore throat of $195 \mu\text{m}$ radius was probably measured at the surface of the rock core where the drilling process affected the pore space. The pore throat distribution for our Clashach sandstone sample was very similar to the pore throat distribution for Berea sandstone [57]. Compared to the pore throat distributions for Bentheimer sandstone and

Doddington sandstone [57], our Clashach sandstone sample showed smaller pore throat sizes. Limestones generally show a wider pore throat size distributions than sandstones [57].

H_2 flow behaviour and trapping mechanisms

Hydrogen behaved as a non-wetting phase, filling the centre of the pores, with residual brine in the pore corners and throats (Fig. 3b and c), indicating a water wetting system. The largest H_2 cluster was much larger than discrete pores at any pore fluid pressure during drainage (Fig. 5), indicating a good connectivity of the H_2 [58]. Hydrogen trapping occurred via snap-

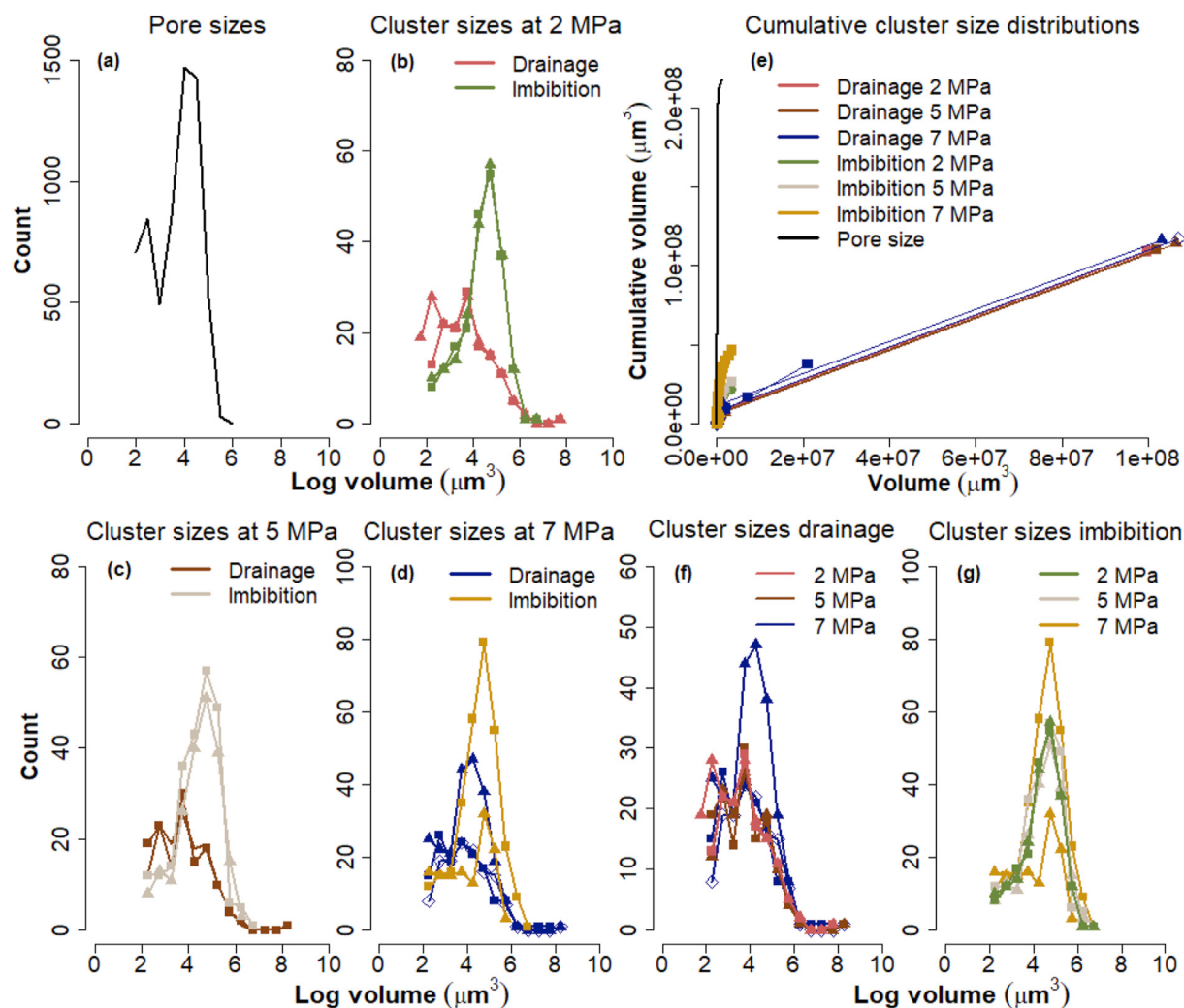


Fig. 5 – (a) Pore size distribution as derived from the micro-CT image of the water-wet rock. Hydrogen cluster size distributions after drainage and imbibition in experiments at $20 \mu\text{m} \text{min}^{-1}$ flowrate and pore fluid pressures of 2 MPa (b), 5 MPa (c) and 7 MPa (d), and cumulative pore size and H_2 cluster size distributions at different pore fluid pressures (e), where squares, triangles and rhombi mark the distinct repeat experiments. (f) Hydrogen cluster size distribution after drainage for all experiments and (g) Hydrogen cluster size distribution after imbibition for all experiments. Note the large H_2 clusters of $\sim 10^8 \mu\text{m}^3$ that exist after drainage in (b)–(d). A decrease in the biggest cluster volume after imbibition in (b)–(d) along with an increase in the number of small clusters marks the change in H_2 structure during the drainage and imbibition processes. Histogram plots in (a)–(d), (f) and (g) used a bin size of 10.

off of H_2 ganglia (Fig. 9). Snap-off competes with piston-like, i.e. pore-filling, displacement during the displacement of a non-wetting fluid by a wetting fluid in porous media, and is known as the swelling of water in the corner layers of a pore throat during water invasion in water-wet porous rocks until the threshold capillary pressure is exceeded, resulting in spontaneous filling of the throat with water and disconnection of the non-wetting phase which can lead to trapping [58,59]. Brine films around grains were not directly visible in the tomographic images (Fig. 3b and c) but were revealed by subtraction of the water-wet scan from the brine-saturated scan after H_2 injection, following the registration of the brine-saturated scan after H_2 injection to the water-wet scan (Fig. 3d and e). Fig. 3d and e suggest that brine films were discontinuous and very thin. When H_2 was injected into a dry

rock, 100% of the injected H_2 could be recovered (Fig. 8e) which substantiated the theory that sub-resolution brine films around grains and snap-off of H_2 ganglia caused decreased H_2 recovery in experiments using an initially brine saturated rock (UoE experiments). The occurrence of several very small H_2 bubbles in the dry-rock experiment (Fig. 8d) indicated Roof snap-off [60] of H_2 ganglia

Effect of pore fluid pressure and hydrogen/brine injection ratio

We observed no dependence of the H_2 saturation during drainage on pore fluid pressure, considering that 2 out of 3 experiments at 7 MPa showed the same H_2 saturation of $\sim 50\%$ as at 2 and 5 MPa (Fig. 4a–c, f, and Fig. A3). The one experiment

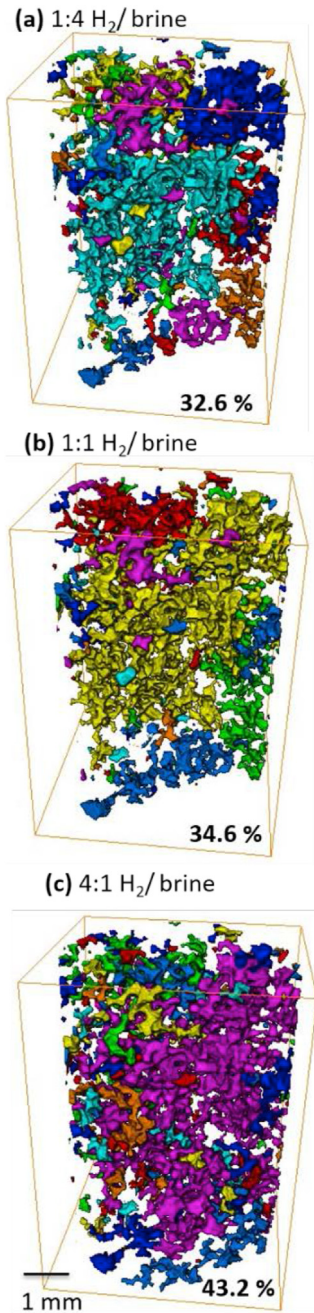


Fig. 6 – Effect of H₂/brine injection ratio on H₂ saturation and H₂ connectivity during simultaneous H₂ and brine injection at 5 MPa (a) 4 $\mu\text{l min}^{-1}$ H₂ plus 16 $\mu\text{l min}^{-1}$ brine, (b) 10 $\mu\text{l min}^{-1}$ H₂ plus 10 $\mu\text{l min}^{-1}$ brine, (c) 16 $\mu\text{l min}^{-1}$ H₂ plus 4 $\mu\text{l min}^{-1}$ brine. Discrete H₂ clusters were rendered in colors, where mainly one color marks one large, connected cluster and different colors indicate several, not connected clusters. With increasing injection ratio H₂ saturation and H₂ connectivity increase. (For interpretation of the references to color/colour in this figure legend, the reader is referred to the Web version of this article.)

at 7 MPa which had only 39.7% H₂ saturation (Fig. 4c, Fig. A3 and blue triangles in Fig. 5f) did also not have the same H₂ cluster size distribution as the remaining experiments (Fig. 5f),

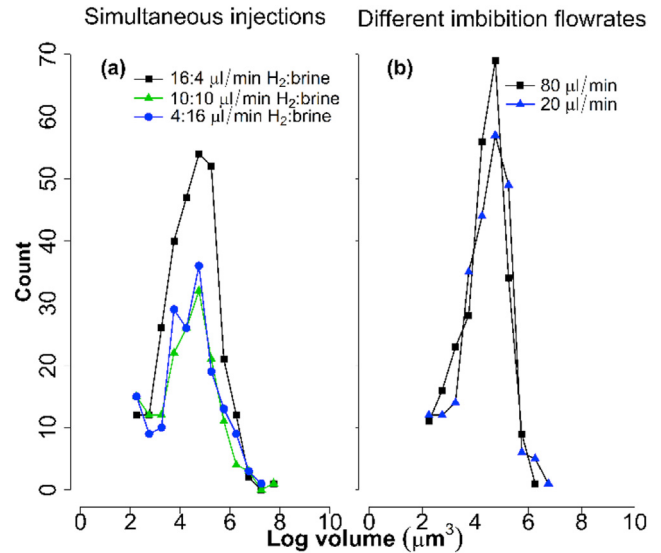


Fig. 7 – (a) H₂ cluster size distributions during simultaneous injections of H₂ and brine at flowrate ratios of 16:4, 10:10 and 4:16 $\mu\text{l min}^{-1}$ H₂:brine and 5 MPa injection pressure. As the flowrate ratio of H₂ to brine increased, the number of intermediate size H₂ clusters increased and the volume of the biggest cluster increased. (b) Effect of flowrate during brine imbibition. All plots used a bin size of 10.

despite using the same experimental settings as for all other experiments at 7 MPa, and the log archives of the pore fluid pressures and injected volumes revealed no abnormalities. A shift in the distribution of cluster sizes can indicate a change in wettability, regardless of the measured H₂ saturation. Yet, as two of the results at 7 MPa showed a similar distribution as at the other pressures, it seems likely that this experiment is an outlier. The experiment was acquired after a filament change on the μCT apparatus, which implied that a slightly different part of the same rock core was imaged (13.6% vs. 12.5% porosity). Yet, in principle this should not have affected the results significantly, and subsequent experiments did return to show $\sim 50\%$ H₂ saturation, e.g. the H₂ stability experiment (Fig. A2).

The observed constant drainage H₂ saturations with increasing pore fluid pressures from 2 to 7 MPa are in line with a lack of a dependence of the H₂ wettability on pressure increases from 2 to 10 MPa in Berea and Bentheimer sandstone [22], with only very small increases of $\sim 3\text{--}6^\circ$ in the H₂ contact angles at pressure increases from 2 to 7 MPa in Basalt [25], clay [28] and quartz [23], and with previous findings of no change in the characteristic trapping curves for CO₂ and N₂ at a wide range of pressure and temperature conditions [37]. The general anticipation of an increase in gas saturation with injection pressure [61,62] may still be valid over pressure ranges larger than the one investigated here. At unchanged wettability, the S_{nwi} is controlled by the capillary pressure which in turn is controlled either by the fractional flow (during simultaneous injection) or by the viscous force pressure drop (during single fluid phase injection). Thus, the independence of the S_{nwi} from the pore fluid pressure indicates that the viscous pressure drop

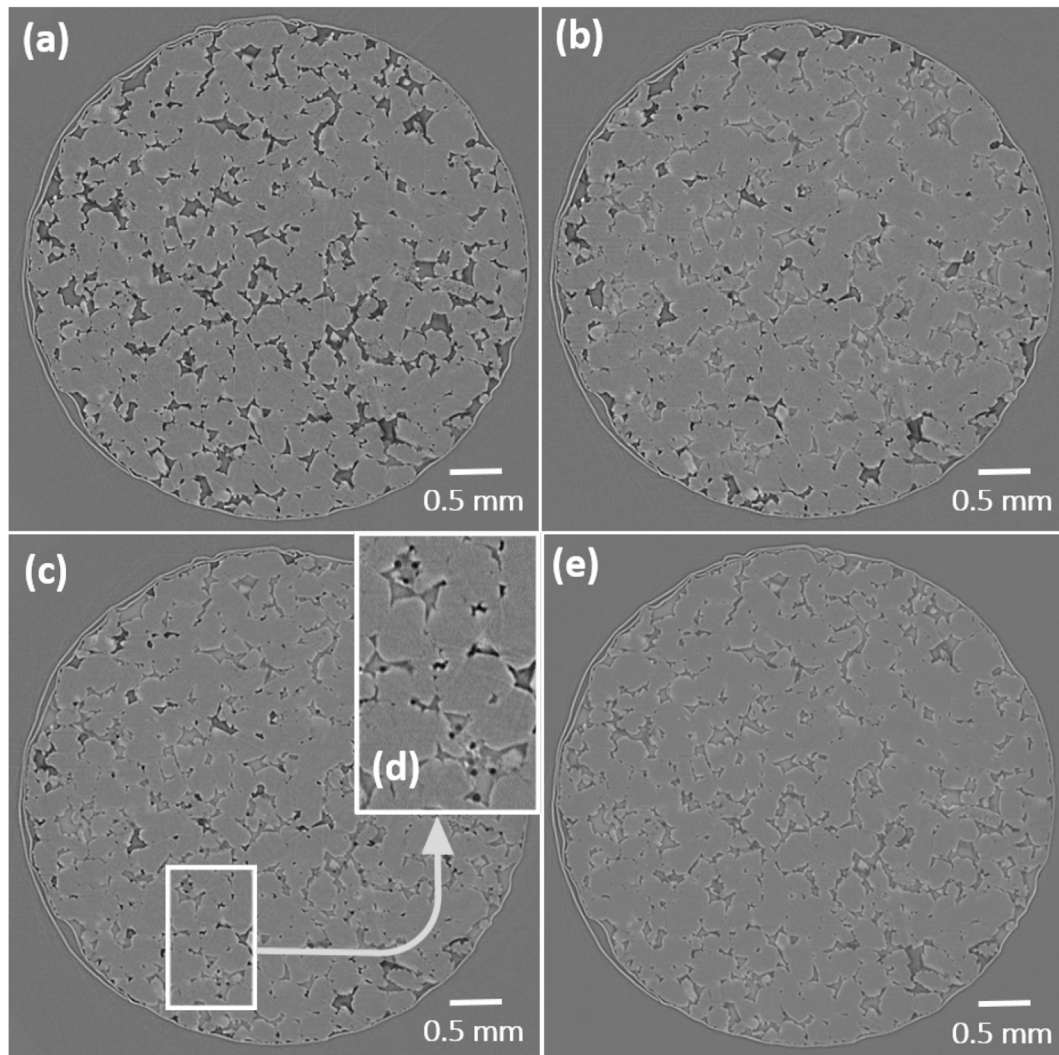


Fig. 8 – The dry-rock experiment summarized. (a) H₂-saturated, dry rock, (b) scan during brine imbibition shortly after appearance of the first brine in the rock, (c) scan during brine imbibition after 115 min, with several small, isolated H₂ bubbles inside pore bodies (d), and (e) brine-saturated rock after 2 h of imbibition showing 100% recoverability of H₂.

is not being significantly altered by the changing pressure, e.g., the H₂ viscosity change is not having a major impact on the force required to drive flow. Significant loss of H₂ from the gas phase at higher pressures by dissolution into the brine is precluded by the low solubility of H₂ of $\sim 0.02 \text{ mol kg}^{-1}$ at 2.5 MPa [63]. The H₂ stability experiments showed that H₂ saturation at 5 MPa did not change over a time period of 10 h (49.55% at time zero vs. 49.53% 10 h after; Fig. A2), evidencing a stable result and no H₂ loss by dissolution. Recent reports of a significantly increased S_{nwr} when using H₂-equilibrated brine over non H₂-equilibrated brine in H₂ and brine displacement experiments in Bentheimer sandstone at 10 MPa and 50 °C [44], indicate that employing a combination of high temperature and pressure causes significant dissolution of H₂.

Looking at the S_{nwr} data only (Fig. 4a–c,f), there was no clear dependency on pore fluid pressure during imbibition. Any change may, however, have been masked by the high variation between the two results at 7 MPa (4–21% Fig. 4c and f). Considering that the experiment at 7 MPa with the low S_{nwi} of 40% was identified as an outlier (see the discussion above 4.3

and Fig. 5f, blue triangles) and that the S_{nwr} is a function of the S_{nwi} where a lower S_{nwi} will tend to overestimate recovery [57,64], we may disregard the S_{nwr} of 4%. The large increase in trapped H₂ in the second full primary drainage and secondary imbibition experiment at 7 MPa (Fig. 4f) was probably due to the poorer initial H₂ connectivity [64]. The H₂ cluster size distribution for this experiment showed an increase in the number of intermediate size clusters compared to the other experiments (Fig. 5g, dark yellow squares), without however shifting the cluster distribution, suggesting no wettability change. This indicates that variation in one or more of the other thermophysical properties – density, viscosity, or IFT – have resulted in the impact on the pore scale fluid configuration (Fig. 10). Meanwhile, a poorer initial H₂ connectivity was not confirmed by the third repetition of primary drainage at 7 MPa (Fig. A3g). More experiments at 7 MPa are needed to confirm the result of increased trapping at higher pore fluid pressures.

Given a hydrostatic gradient of $\sim 10 \text{ MPa/km}$ an increase of the S_{nwr} with increasing pore fluid pressure, as suggested by

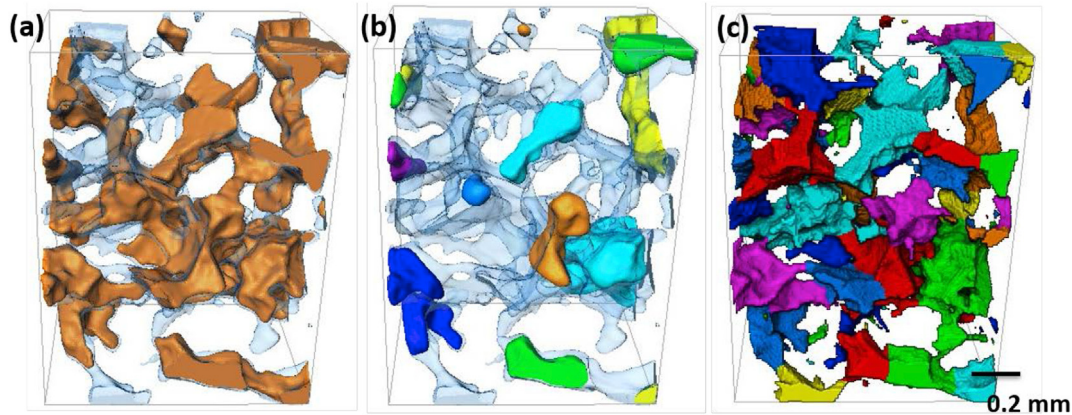


Fig. 9 – Example of a snap-off event. (a) Labelled H₂-filled volume after drainage (orange), spanning over several pores and showing one large interconnected H₂-filled pore volume, and total pore space (transparent blue). (b) Labelled H₂-filled volume after brine imbibition (different coloured shades) and the total pore space (transparent blue) showing several, not connected H₂ ganglia and a snapped-off H₂ droplet (cobalt blue) in the centre, left hand side. (c) Pore body visualization of the same volume. (For interpretation of the references to color/colour in this figure legend, the reader is referred to the Web version of this article.)

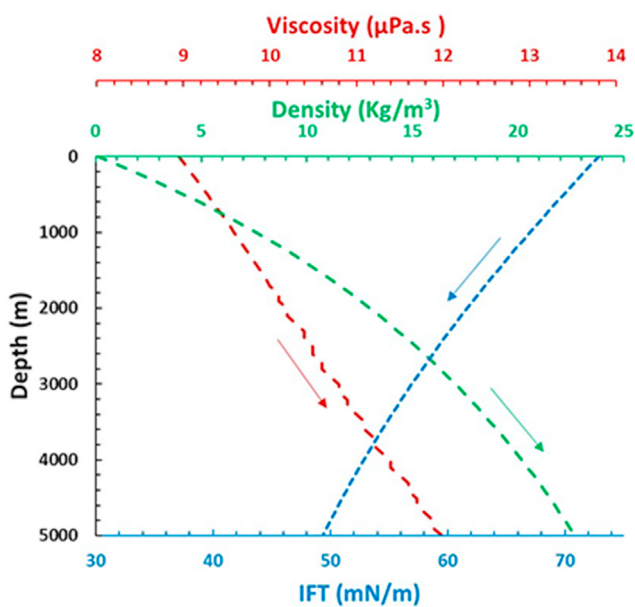


Fig. 10 – Density (green line), viscosity (red line), and interfacial tension (blue line) of hydrogen versus depth (Hassanpouryouzband et al., 2021) [65]. (For interpretation of the references to color/colour in this figure legend, the reader is referred to the Web version of this article.)

the second experiment at 7 MPa (Fig. 4f), would indicate that deeper aquifers are less favourable for H₂ storage operations. However, unlike our unsteady state experiments which showed barely any pressure difference between inlet and outlet, in a real H₂ storage operation, the well pressure is significantly higher than the reservoir pressure and the brine is not injected, but naturally flowing into previously H₂-saturated rock when the H₂ is recovered again, due to a pressure difference. Our displacement study results are hence applicable to the fringe of the H₂-saturated zone, only, where

pressure differences are very small. A decreased H₂ recovery with depth would not align well with other criteria for an economical and safe H₂ storage operation, such as a lower cushion gas requirement with elevated depth [5] and reduced risks for H₂-linked microbial activity at higher depths due to higher temperatures [6].

The pressure/depth effect on our results can be further related to the variation of key pore-scale displacement parameters for H₂ with depth (Fig. 10): The IFT of H₂ reduces with depth whereas the H₂ viscosity increases, both of which in theory should augment the displacement of H₂ with water and reduce the S_{nwr} [66,67]. However, increased S_{nwr} with decreasing IFT and increasing viscosity has also been demonstrated [68] which may be due to a simultaneously increased likelihood of unstable displacement/non-uniform fronts [69,70] during both drainage and imbibition processes at decreasing IFT and increasing viscosity, based on the augmenting effect of both parameters on N_c (Eq. (1)). Such unstable displacement processes at higher pore fluid pressures, addition to a variation in the thickness of the brine thin films with pressure, may explain the decrease in interconnected H₂-filled pore volume from one large cluster at 2–5 MPa to three clusters at 7 MPa and have led to increased snap-off and trapping during imbibition (Fig. 4f).

The S_{nwr} of 10–21% was significantly lower than the previously reported H₂ S_{nwr} of 41% for a Gosford sandstone under ambient conditions [42] but in line with 20–25% H₂ S_{nwr} in a Bentheimer sandstone at 10 MPa and 50 °C [44]. As mentioned previously, the short length rock sample in Jha et al. (2021) [42] suggests that their results were affected by capillary end effects [49]. However, the relatively high bulk N_c of $2.3\text{--}2.4 \times 10^{-6}$ during brine imbibition in our experiments and those of Jangda et al. (2022) [44] may have mobilized more residual H₂ than under strict capillary regime conditions. Our results are higher than previously reported S_{nwr} of <2% in a Fontainebleau sandstone at 0.4 MPa, ambient temperature and bulk N_c of 3.5×10^{-8} [41], however the S_{nwr} in this study was extremely low (4%).

During simultaneous injection of H₂ and brine, which may be representative of H₂ injection into hydrodynamic aquifers or simulate the far field conditions, H₂ saturation and H₂ interconnected pore volume increased with increasing H₂/brine injection ratio (Fig. 6). This indicated that a lower brine flow is favoured over high flow environments in terms of optimising the H₂ storage operation. The structure was apparently not percolating in any of the simultaneous injection experiments as opposed to during 100% H₂ injection (Fig. 6 vs. Fig. 4b), yet considering significant pressure differences of up to 0.05 MPa between inlet and outlet in simultaneous injection experiments which were not observed in experiments injecting 100% H₂, the connections between the H₂ clusters may have been broken when the injection (and thereby the pressure gradient) was stopped for the scan.

Effect of capillary number on initial and residual saturation

Classical pore-scale displacement theory predicts little change in residual phase saturation in response to increases in flow rate until the N_C exceeds 10^{-6} – 10^{-5} . However, for most subsurface reservoirs there will be rapid decreases at N_C of 10^{-4} or more, when viscous forces become dominant [57]. The bulk brine N_C applied in this study (2.4 – 9.4×10^{-6}) was within the range of little saturation change but exceeded the threshold of $N_C < 10^{-6}$ for which the flow generally is said to be capillary dominated [57]. This may indicate that viscous forces caused a significant effect of N_C on the S_{nwr} in our experiments (Fig. 4b and d), and these forces are likely to be even greater at local scale than at bulk [57]. The H₂ cluster size distribution after imbibition at $N_C = 9.4 \times 10^{-6}$ was shifted with respect to the distribution at $N_C = 2.4 \times 10^{-6}$ (Fig. 7b), indicating a change in the wetting behaviour and supporting previous findings of preferential desaturation of larger clusters at higher N_C [71].

We observed a 4% decrease in S_{nwi} in our experiments when bulk N_C was increased from 1.7×10^{-8} to 6.8×10^{-8} (Fig. 4b and d). Critical nonwetting phase N_C of 2×10^{-8} and 10^{-5} during imbibition have been reported for water–gas systems and water–oil systems, respectively [72], indicating that the threshold of $N_C < 10^{-6}$ for capillary dominated flow [57] is not rigid. However, considering reported increases in the H₂ saturation after drainage with increasing N_C from 7.7×10^{-7} to 7.7×10^{-5} [24], and acknowledging the small observed difference in S_{nwi} , we cannot exclude that the effect of flow rate was down to experimental variability.

Comparison to nitrogen

The N₂ saturation was comparable to the H₂ saturation during drainage at similar N_C of 1 – 3×10^{-8} but the S_{nwr} after imbibition was ~20% higher for N₂ than for H₂ (Fig. 4b and e). Using N₂ as a proxy for H₂ in experimental drainage and imbibition studies is hence not advisable. Considering the high degree of N₂ trapping, the use of N₂ as a cushion gas for H₂ storage operations which could reduce operational costs [7] seems favourable. Our results are lower than a reported 64% N₂ S_{nwi} after drainage and 43% N₂ S_{nwr} in a Berea sandstone (20–22% porosity) at 5.5 MPa and 20 °C [39], and higher than 43% N₂ S_{nwi} in a Bashijiqike tight sandstone (5.6% porosity) at 8 MPa and ambient temperature [38]. The trend in

the differences of the N₂ saturation in the above studies follows the same trend as the differences in the porosities of the studied sandstones, with the Clashach sandstone (14% porosity) being intermediate between the two other rocks. This indicates that porosity differences between the different rock types applied in the above experiments defined the observed N₂ saturations, yet differences in the pore throats dimensions may equally have contributed or caused this. It also suggests that S_{nwi} and S_{nwr} depend strongly on (the local conditions within) each rock, and that these rock type/local effects may mask any effect of injection conditions, whereas trends in the rock-specific behaviour will be controlled by pressure and flow conditions. Meanwhile observations of N₂ S_{nwi} and S_{nwr} of 15–26% and 8–17%, respectively, in a Fontainebleau sandstone with 9.7% porosity at 0.4 MPa, ambient temperature and N_C of 3.5×10^{-8} to 7×10^{-7} [41] do not confirm the relation between initial and residual saturations and porosity. This suggests that other parameters such as the absolute permeability of a rock also shape the rock specific response to N₂ and brine displacement processes. More studies on different types of rock and under similar injection conditions are needed to better understand the rock-specific differences in S_{nwi} and S_{nwr} .

Suitability of the Clashach sandstone for hydrogen storage

It has been postulated that the low viscosity of H₂ will cause the gas to travel swiftly, making it unsuitable for displacing brine [69] and causing low H₂ injectivity. In this work, we showed that from an injectivity and recovery perspective, untreated Clashach sandstone is suitable for underground H₂ storage. However, sandstones aged by exposure to humic acids may be more suitable analogue rocks for experimental investigations of H₂ storage in porous media [23]. Considering that aging has previously been shown to alter the wettability of H₂ brine–quartz systems from highly water-wet toward intermediate-wet [23] the stated H₂ saturations for our untreated outcrop Clashach sandstone are expected to increase during drainage and decrease during imbibition, further the increasing suitability for H₂ storage.

Conclusion

In this work, a prima facie examination of H₂ flow and displacement processes in porous rock was carried out as a function of capillary numbers of 1.2 – 6.8×10^{-8} for H₂ and 2.4 – 9.5×10^{-6} for brine, and of pore fluid pressures between 2–7 MPa. Results showed no clear influence of pore fluid pressure on H₂ saturation during drainage in the investigated pressure range, with ~50% of the pore space saturated with H₂ during drainage at all pressures. During imbibition, 20%, 22% and 43% of the initially injected H₂ was trapped at 2, 5 and 7 MPa, respectively, and a capillary number of 2.4×10^{-6} , indicating that higher pressure, i.e. deeper reservoirs are less favourable for H₂ storage. Injection of brine at higher capillary numbers reduced capillary trapping and increased H₂ recovery. Hydrogen recovery was distinct from N₂ recovery, suggesting that N₂ is a poor proxy for H₂. Based on these results, we

recommend more shallow, lower pressure sites for future H₂ storage operations in porous media.

Future work should aim to measure the influence of pressures above 7 MPa, elevated temperatures and rock aging on H₂ and brine displacement processes at a range of different capillary numbers and in different porous formations. Closer characterization of the pore space in terms of connectivity (Euler number), absolute and relative permeability, tortuosity and pore size could give further insight to understanding rock-specific responses during drainage and imbibition. Dynamic experiments using synchrotron light sources are recommended to examine displacement mechanisms closely. The presented experimental setup is suitable for investigating gas and brine displacement processes in a variety of porous samples, and is only limited by size of the pore matrix due to the resolution requirements of the μ -CT scanner.

Author contributions

The experimental kit was built by Butler and Thaysen. Experiments were carried out by Thaysen, Butler, Hassanpouryouzband, Freitas. Alvarez-Borges and Atwood were the supporting beamline scientists during the experiments at Diamond Light Source. Image reconstruction and tomographic analysis was carried out by Thaysen. Interpretation of the results was by Thaysen, Butler, Hassanpouryouzband, Krevor and Heinemann. The manuscript was written by Thaysen with review by Butler, Krevor, Heinemann, Hassanpouryouzband, Freitas and Edlmann. All authors have given approval to the final version of the manuscript.

Funding sources

Thaysen, Butler, Hassanpouryouzband, Heinemann and Edlmann gratefully acknowledge the funding support from the Engineering and Physical Science Research Council (EPSRC) HyStorPor project [grant number EP/S027815/1] and from the Fuel Cells and Hydrogen 2 Joint Undertaking (JU) under grant agreement No 101006632. The JU receives support from the European Union's Horizon 2020 research and innovation programme and Hydrogen Europe and Hydrogen Europe Research. This work was enabled and carried out with the support of Diamond Light Source, Beamline I12-JEEP 101006632 (proposal mg26730-1).

Declaration of competing interest

The authors declare that they have no known competing financial interests or personal relationships that could have appeared to influence the work reported in this paper.

Acknowledgment

We would like to thank Thomas Connolley for any correspondence and help with setting up the experiments at

Diamond Light Source, and Alexis Cartwright-Taylor for assistance and discussions around the experimental results.

Appendix A. Supplementary data

Supplementary data to this article can be found online at <https://doi.org/10.1016/j.ijhydene.2022.10.153>.

REFERENCES

- [1] Tarkowski R. Underground hydrogen storage: characteristics and prospects. *Renew Sustain Energy Rev* 2020;105:86–94.
- [2] Beckingham LE, Winningham L. Critical knowledge gaps for understanding water-rock-working phase interactions for compressed energy storage in porous formations. *ACS Sustainable Chem Eng* 2020;8(1):2–11.
- [3] Mouli-Castillo J, Heinemann N, Edlmann K. Mapping geological hydrogen storage capacity and regional heating demands: an applied UK case study. *Appl Energy* 2021;(116348):283.
- [4] Hassanpouryouzband A, et al. Thermodynamic and transport properties of hydrogen containing streams. *Sci Data* 2020;1(1):1–14.
- [5] Heinemann N, et al. Hydrogen storage in porous geological formations - onshore play opportunities in the Midland Valley (Scotland, UK). *Int J Hydrogen Energy* 2018;43(45):20861–74.
- [6] Thaysen EM, et al. Estimating microbial growth and hydrogen consumption in hydrogen storage in porous media. *Renew Sustain Energy Rev* 2021;151(111481):1–15.
- [7] Heinemann N, et al. Enabling large-scale hydrogen storage in porous media: the scientific challenges. *Energy Environ Sci* 2021;14:853–64.
- [8] Matos CR, Carneiro JF, Silva PP. Overview of large-scale underground energy storage technologies for integration of renewable energies and criteria for reservoir identification. *J Energy Storage* 2019;21:241–58.
- [9] Paterson L. The implications of fingering in underground hydrogen storage. *Int J Hydrogen Energy* 1983;8(1):53–9.
- [10] Flesch S, et al. Hydrogen underground storage-Petrographic and petrophysical variations in reservoir sandstones from laboratory experiments under simulated reservoir conditions. *Int J Hydrogen Energy* 2018;43(45):20822–35.
- [11] Yekta AE, Pichavant M, Audigane P. Evaluation of geochemical reactivity of hydrogen in sandstone: application to geological storage. *J Appl Geochem* 2018;95:182–94.
- [12] Hassanpouryouzband A, et al. Geological hydrogen storage: geochemical reactivity of hydrogen with sandstone reservoirs. *ACS Energy Lett* 2022;7:2203–10.
- [13] Veshareh MJ, Thaysen EM, Nick HM. Feasibility of hydrogen storage in depleted hydrocarbon chalk reservoirs: assessment of biochemical and chemical effects. *Appl Energy* 2022;323(119575):1–11.
- [14] Labus K, Tartowski R. Modeling hydrogen – rock – brine interactions for the Jurassic reservoir and cap rocks from Polish Lowlands. *Int J Hydrogen Energy* 2022;47(20):10947–62.
- [15] Boon M, Hajibeygi H. Experimental characterization of H₂/water multiphase flow in heterogeneous sandstone rock at the core scale relevant for underground hydrogen storage (UHS). *Nat Sci Rep* 2022;12(14604):1–11.
- [16] Yekta AE, et al. Determination of hydrogen-water relative permeability and capillary pressure in sandstone: application to underground hydrogen injection in sedimentary formations. *Transport Porous Media* 2018;122(2):333–56.

- [17] Rezaei A, et al. Relative permeability of hydrogen and aqueous brines in sandstones and carbonates at reservoir conditions. *Geophys Res Lett* 2022;49:1–9.
- [18] Lysyy M, et al. Hydrogen relative permeability hysteresis in underground storage. *Geophys Res Lett* 2022;49:1–8.
- [19] Higgs S, et al. In-situ hydrogen wettability characterisation for underground hydrogen storage. *Int J Hydrogen Energy* 2021;47(26):13062–75.
- [20] Esfandyari H, et al. Experimental evaluation of rock mineralogy on hydrogen-wettability: implications for hydrogen geo-storage. *J Energy Storage* 2022;52(104866):1–8.
- [21] Hosseini M, et al. Assessment of rock-hydrogen and rock-water interfacial tension in shale, evaporite and basaltic rocks. *J Nat Gas Sci Eng* 2022;106(104743):1–8.
- [22] Hashemi L, et al. Contact angle measurement for hydrogen/brine/sandstone system using captive-bubble method relevant for underground hydrogen storage. *Adv Water Resour* 2021;154(103964):1–13.
- [23] Iglauer S, Muhammad A, Keshavarz A. Hydrogen wettability of sandstone reservoirs: implications for hydrogen geo-storage. *Geophys Res Lett* 2020;48(3):1–5.
- [24] Lysyy M, Ersland G, Fernø M. Pore-scale dynamics for underground porous media hydrogen storage. *Adv Water Resour* 2022;163(104167):1–13.
- [25] Al-Yaseri A, Jha NK. On hydrogen wettability of basaltic rock. *J Pet Sci Eng* 2021;200:1–5.
- [26] Hosseini M, et al. Basalt-H₂-brine wettability at geo-storage conditions: implication for hydrogen storage in basaltic formation. *J Energy Storage* 2022;52(104745):1–6.
- [27] van Rooijen W, et al. Microfluidics-based analysis of dynamic contact angles relevant for underground hydrogen storage. *Adv Water Resour* 2022;164(104221):1–17.
- [28] Al-Yaseri A, et al. Hydrogen wettability of clays: implications for underground hydrogen storage. *Int J Hydrogen Energy* 2021;46(69):34356–61.
- [29] Azin R, Izadpanahi A. In: Oluyemi G, et al., editors. *Fundamentals and practical aspects of gas injection*. Springer; 2022.
- [30] Morrow N, Chatzis I, Taber JJ. Entrapment and mobilization of residual oil in bead packs. *SPE Reservoir Eng* 1988;3(3).
- [31] Blunt MJ, et al. Pore-scale imaging and modelling. *Adv Water Resour* 2013;51:197–216.
- [32] Saraf S, Bera A. A review on pore-scale modeling and CT scan technique to characterize the trapped carbon dioxide in impermeable reservoir rocks during sequestration. *Renew Sustain Energy Rev* 2021;144(110986):1–20.
- [33] Iglauer S, et al. Residual CO₂ imaged with x-ray micro-tomography. *Geophys Res Lett* 2011;38(L21403):1–6.
- [34] Andrew M, Bijeljic B, Blunt MJ. Pore-scale imaging of trapped supercritical carbon dioxide in sandstones and carbonates. *Int J Greenh Gas Control* 2014;22:1–14.
- [35] Rahman T, et al. Residual trapping of supercritical CO₂ in oil-wet sandstone. *J Colloid Interface Sci* 2016;469:63–8.
- [36] Krevor SCM, et al. Relative permeability and trapping of CO₂ and water in sandstone rocks at reservoir conditions. *Water Resour Res* 2012;48:1–16.
- [37] Niu B, Al-Menhali A, Krevor SC. The impact of reservoir conditions on the residual trapping of carbon dioxide in Berea sandstone. *Water Resour Res* 2015;51(4):2009–29.
- [38] Cao Q, et al. Pore-scale simulations of gas storage in tight sandstone reservoirs for a sequence of increasing injection pressure based on micro-CT. *J Nat Gas Sci Eng* 2019;64:15–27.
- [39] Khishvand M, Alizadeh AH, Piri M. In-situ characterization of wettability and pore-scale displacements during two- and three-phase flow in natural porous media. *Adv Water Resour* 2016;97:270–98.
- [40] Sarmadivaleh M, Al-Yaseri A, Iglauer S. Influence of temperature and pressure on quartz–water–CO₂ contact angle and CO₂–water interfacial tension. *J Colloid Interface Sci* 2015;441:59–64.
- [41] Al-Yaseri A, et al. Initial and residual trapping of hydrogen and nitrogen in Fontainebleau sandstone using nuclear magnetic resonance core flooding. *Int J Hydrogen Energy* 2022;47(53):22482–94.
- [42] Jha NK, et al. Pore scale investigation of hydrogen injection in sandstone via X-ray micro-tomography. *Int J Hydrogen Energy* 2021;46:34822–9.
- [43] Pak T, et al. Droplet fragmentation: 3D imaging of a previously unidentified pore-scale process during multiphase flow in porous media. *Proc Natl Acad Sci U S A* 2015;112(7):1947–52.
- [44] Jangda Z, et al. Pore-scale visualization of hydrogen storage in a sandstone at subsurface pressure and temperature conditions: trapping, dissolution and wettability. *J Colloid Interface Sci* 2022;629(B):316–25.
- [45] Iglauer S, et al. Comparison of residual oil cluster size distribution, morphology and saturation in oil-wet and water-wet sandstone. *J Colloid Interface Sci* 2012;375:187–92.
- [46] Iglauer S, Paluszny A, Blunt MJ. Simultaneous oil recovery and residual gas storage: a pore-level analysis using in situ X-ray micro-tomography. *Fuel* 2013;103:905–14.
- [47] Pentland, C.H., et al., *Capillary trapping in water-wet sandstones: coreflooding experiments and pore-network modeling*, in SPE international 2010, Society of Petroleum Engineers Florence, Italy
- [48] Fousseis F, et al. A low-cost X-ray-transparent experimental cell for synchrotron-based X-ray microtomography studies under geological reservoir condition. *J Synchrotron Radiat* 2014;21(1):251–3.
- [49] Pak T. Saturation tracking and identification of residual oil saturation. University of Edinburgh; 2014.
- [50] Kumar M, et al. Mapping fluid distributions in 3D at the pore scale: quantifying the influence of wettability and saturation history on rock resistivity. In: SPWLA 50th annual logging symposium. Society of Petrophysicists and Well-Log Analysts; 2009.
- [51] Yusibani E, et al. A capillary tube viscometer designed for measurements of hydrogen gas viscosity at high pressure and high temperature. *Int J Thermophys* 2011;32(6):1111–24.
- [52] Chow YTF, Maitland GC, Trusler JPM. Interfacial tensions of (H₂O + H-2) and (H₂O + CO₂ + H-2) systems at temperatures of (298–448) K and pressures up to 45 MPa. *Fluid Phase Equil* 2018;475:37–44.
- [53] Chow YTF, Maitland GC, Trusler JPM. Erratum to "Interfacial tensions of (H₂O + H-2) and (H₂O + CO₂ + H-2) systems at temperatures of (298–448) K and pressures up to 45 MPa. *Fluid Phase Equil* 2020;503(112315):1.
- [54] Nakai T, et al. Effect of pressure on the viscosity B coefficient of cesium chloride in water. *Mater Sci Res Int* 1996;2(3):143–7.
- [55] Vlassenbroeck J, et al. Octopus 8: a high performance tomographic reconstruction package for X-ray tube and synchrotron micro-CT. In: Desrues J, Viggiani G, Bésuelle P, editors. *Advances in X-ray tomography for geomaterials*. London, UK: ISTE; 2010.
- [56] Buades A, Coll B, Morel JM. A non-local algorithm for image denoising. 2005 IEEE computer society conference on computer vision and pattern recognition (CVPR'05). 2005.
- [57] Blunt, M.J., *Multiphase flow in permeable media. A Pore-scale perspective* 2017, Cambridge, United Kingdom: Cambridge University Press
- [58] Singh K, et al. Dynamics of snap-off and porefilling events during two-phase fluid flow in permeable media. *Sci Rep* 2017;7(5192):1–13.

- [59] Krevor S, et al. Capillary trapping for geologic carbon dioxide storage – from pore scale physics to field scale implications. *Int J Greenh Gas Control* 2015;40:221–37.
- [60] Roof JG. Snap-off of oil droplets in water-wet pores. *Soc Petrol Eng J* 1970;10(1):85–90.
- [61] Thomas LK, Katz DL, Tek MR. Threshold pressure phenomena in porous media. *Soc Petrol Eng J*; 1968. p. 174–84.
- [62] Boone MA, et al. 3D mapping of water in oolitic limestone at atmospheric and vacuum saturation using X-ray micro-CT differential imaging. *Mater Char* 2014;97:150–60.
- [63] De Lucia M, et al. Measurements of H₂ solubility in saline solutions under reservoir conditions: preliminary results from project H₂STORE. *European Geosciences Union General Assembly 2015 Division Energy, Resources and Environment, Egu* 2015;76:487–94. 2015.
- [64] Herring AL, et al. Effect of fluid topology on residual nonwetting phase trapping: implications for geologic CO₂ sequestration. *Adv Water Resour* 2013;62:47–58.
- [65] Hassanpouryouzband A, et al. Offshore geological storage of hydrogen: is this our best option to achieve Net-zero? *ACS Energy Lett* 2021;6(6):2181–6.
- [66] Wagner OR, Leach RO. Effect of interfacial tension on displacement efficiency. *SPE J* 1966;6(4):335–44.
- [67] Avraam DG, Payatakes AC. Flow mechanisms, relative Permeabilities, and coupling effects in steady-state two-phase flow through porous media. The case of strong wettability. *Ind Eng Chem Res* 1999;38:778–86.
- [68] Cho J, et al. Effects of relative permeability change resulting from interfacial tension reduction on vertical sweep efficiency during the CO₂-LPG hybrid EOR process. *Energy Sources* 2018;40(10):1242–9.
- [69] Chaturvedi KR, et al. Air foams for mobility control and subsurface storage of hydrogen in porous media: an experimental study. *Energy Fuels* 2022;36:5036–46.
- [70] Sabet N, Hassanzadeh H, Abedi J. Stability of Gravitationally unstable Double diffusive Transient boundary layers with variable viscosity in porous media. *AIChE J* 2017;63(6):2471–82.
- [71] Oughanem R, et al. Pore-scale to core-scale study of capillary desaturation curves ulti multi-scale 3D imaging in International Symposium of the Society of Core Analysts. USA: Napa Valley, California; 2013.
- [72] Ding M, Kantzas A. Capillary number correlations for gas-liquid systems. *J Can Petrol Technol* 2007;46(27–32).